

Laboratory triggering of stick-slip events by oscillatory loading in the presence of pore fluid with implications for physics of tectonic tremor

N. M. Bartlow,¹ D. A. Lockner,² and N. M. Beeler²

Received 14 May 2012; revised 26 September 2012; accepted 10 October 2012; published 28 November 2012.

[1] The physical mechanism by which the low-frequency earthquakes (LFEs) that make up portions of tectonic (also called non-volcanic) tremor are created is poorly understood. In many areas of the world, tectonic tremor and LFEs appear to be strongly tidally modulated, whereas ordinary earthquakes are not. Anomalous seismic wave speeds, interpreted as high pore fluid pressure, have been observed in regions that generate tremor. Here we build upon previous laboratory studies that investigated the response of stick-slip on artificial faults to oscillatory, tide-like loading. These previous experiments were carried out using room-dry samples of Westerly granite, at one effective stress. Here we augment these results with new experiments on Westerly granite, with the addition of varying effective stress using pore fluid at two pressures. We find that raising pore pressure, thereby lowering effective stress can significantly increase the degree of correlation of stick-slip to oscillatory loading. We also find other pore fluid effects that become important at higher frequencies, when the period of oscillation is comparable to the diffusion time of pore fluid into the fault. These results help constrain the conditions at depth that give rise to tidally modulated LFEs, providing confirmation of the effective pressure law for triggering and insights into why tremor is tidally modulated while earthquakes are at best only weakly modulated.

Citation: Bartlow, N. M., D. A. Lockner, and N. M. Beeler (2012), Laboratory triggering of stick-slip events by oscillatory loading in the presence of pore fluid with implications for physics of tectonic tremor, *J. Geophys. Res.*, *117*, B11411, doi:10.1029/2012JB009452.

1. Introduction

[2] Previous studies have shown that earthquakes do not correlate well with the solid earth tides in most environments [e.g., *Heaton*, 1982; *Vidale et al.*, 1998], unless the tides are unusually strong [e.g., *Wilcock*, 2001; *Cochran et al.*, 2004]. Tectonic tremor, however, has been shown to be significantly modulated by tidal stresses in Shikoku, Japan and Cascadia [*Shelly et al.*, 2007; *Nakata et al.*, 2008; *Rubinstein et al.*, 2008; *Thomas et al.*, 2009]. The physical basis of tectonic tremor is not well understood. The sensitivity to tidal loading illuminates a fundamental physical difference between earthquakes and tremor, or the environments they occur in, that has the potential to further our understanding of tremor as a phenomenon. By studying this triggering in the laboratory, we may constrain the range of physical

parameters and stress states that give rise to tidal triggering, which must include the stress state in the tremor region.

[3] Seismic evidence indicates the presence of high, nearly lithostatic fluid pressure at the depth of tremor in multiple subduction zones [*Peacock et al.*, 2011; *Audet et al.*, 2009; *Shelly et al.*, 2006; *Kodaira et al.*, 2004]. This high fluid pressure may reduce effective normal stress, potentially to very low values. In our analysis, we assume that the effective stress law holds:

$$\sigma_{eff} = \sigma_n - \alpha_p P_p \quad (1)$$

Here, σ_{eff} is the effective stress, σ_n is the normal stress, α_p is a scaling factor, and P_p is the pore fluid pressure. For our room temperature experiments, we assume that $\alpha_p = 1$ is appropriate for friction and stick-slip strength [*Byerlee*, 1967]. In the laboratory, earlier studies of laboratory models for tidal triggering were conducted under room dry conditions, without pore fluid, at 10's of MPa normal stresses. It is important to understand how to extrapolate the results of these experiments into the low effective stress, high pore pressure environments of subduction zones. In this study we perform oscillatory triggering experiments using water-saturated samples and controlled pore pressure, at two values of effective stress, as a first step in determining the effect of pore fluid and varying effective stress in tidal triggering.

¹Department of Geophysics, Stanford University, Stanford, California, USA.

²U. S. Geological Survey, Menlo Park, California, USA.

Corresponding author: N. M. Bartlow, Department of Geophysics, Stanford University, Mitchell Building, 397 Panama Mall, Stanford, CA 94305, USA. (noelb@stanford.edu)

©2012. American Geophysical Union. All Rights Reserved.
10.1029/2012JB009452

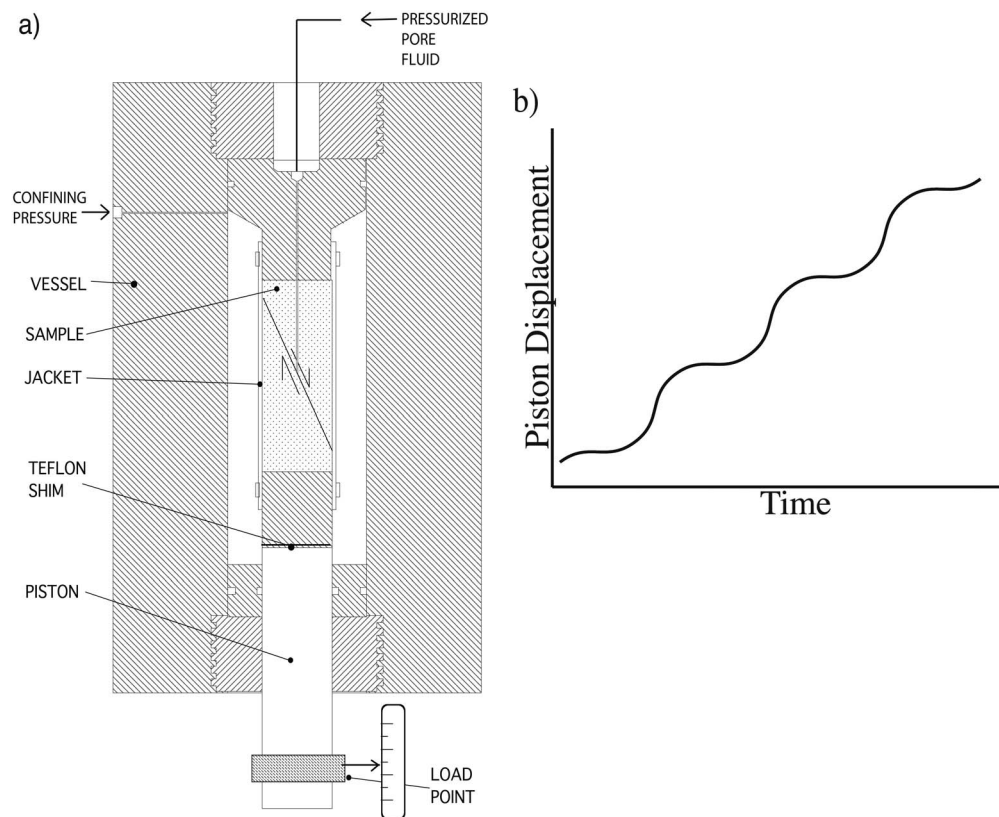


Figure 1. Experimental setup. (a) Schematic cross section of the triaxial loading machine. (b) Schematic diagram of the displacement of the load point in Figure 1a as a function of time. The displacement is a sum of a sinusoid (tidal load) and a line (tectonic load).

[4] This work builds on the previous laboratory oscillatory triggering work of *Lockner and Beeler* [1999], with further analysis in *Beeler and Lockner* [2003], and *Savage and Marone* [2007], summarized here. *Lockner and Beeler* [1999] conducted triaxial loading tests on 3 inch diameter cylindrical samples of westerly granite containing inclined saw cuts, ground flat and roughened to simulate natural faults. The setup of these experiments was very similar to the setup of the experiments presented in this paper (Figure 1). The samples are enclosed in a protective jacket and submerged in a bath of silicon oil which is pressurized to 50 MPa. This provides a uniform confinement pressure on the sample. Additional axial load is applied to the sample by advancing a piston (bottom of Figure 1a) at a controlled rate, called the axial shortening rate. The piston is advanced for a total of approximately 10 mm. This produces between 10 and 31 stick-slip events on the saw cut fault surface for each experiment.

[5] In *Lockner and Beeler* [1999] the axial shortening rate was specified as a sum of a constant rate plus a sinusoidally varying rate, as shown schematically in Figure 1b. This system was taken as a simplified model for a constant tectonic stressing rate plus tidal stresses at a single frequency. The amplitude and frequency of the sinusoidal component were varied with each experiment. The goal of these experiments was to compare the timing of stick-slip events to the sinusoidal loading to see if the events are correlated with the tidal loading component. For each stick-slip event,

the authors recorded the phase of the sine wave component of loading. The phase angle is defined as shown schematically in Figure 2. If this population of phases was sufficiently random, the experiment was declared uncorrelated. If the stick-slip events show a clear clustering around a specific phase, the experiment is declared correlated. Testing of phase populations was done with a Schuster test, described more in section 3. Ultimately, the experiments divided frequency-amplitude space into correlated and uncorrelated regions, with a frequency-dependent correlation boundary. The results for experiments with a constant axial shortening

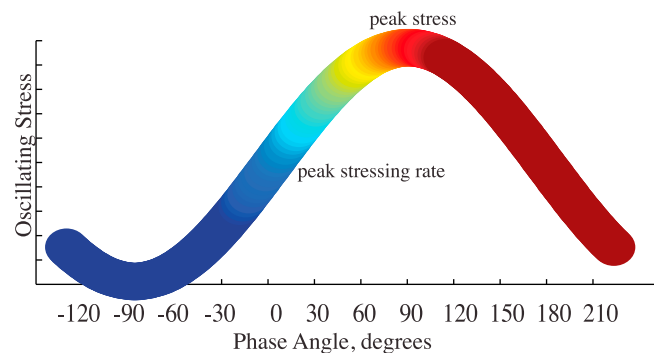


Figure 2. Schematic of oscillatory component of stress, showing phase angles (x-axis) and colors corresponding to Figures 3 and 5.

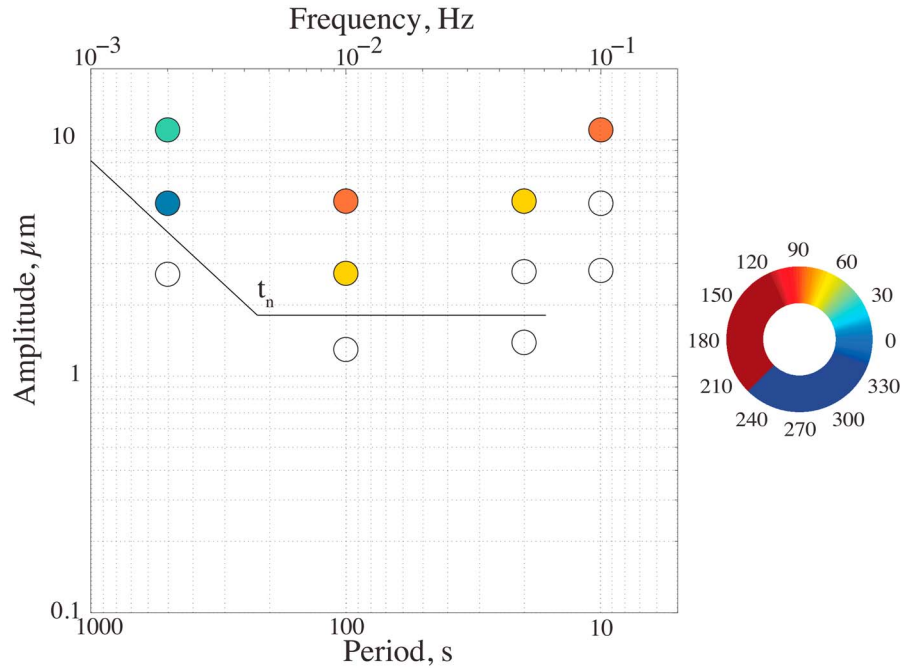


Figure 3. Previous dry, 50 MPa confining pressure experiments results. Open circles represent uncorrelated experiments; colored circles are correlated experiments with color representing correlation phase in degrees as in Figure 2. See color wheel to correspond color to phase angle. Phase angles correspond to a sine wave in displacement; 0° phase is peak shear stress rate and 90° is peak shear stress. The period corresponding to an approximate nucleation time is denoted by t_n . Data and phase analysis from *Beeler and Lockner* [2003].

rate of $0.1 \mu\text{m}$ are reproduced in Figure 3. The black line indicates the correlation boundary.

[6] The analysis presented in *Beeler and Lockner* [2003] of the experiments from *Lockner and Beeler* [1999] built a theoretical framework in which to understand the correlation boundary. Two regimes are discussed. In the first regime, called the Coulomb threshold failure regime, the period of sinusoidal loading is greater than the nucleation time for stick-slip events. In this case, simple Coulomb failure applies and stick-slip occurs when the shear stress reaches a critical value. Stress is most likely to reach this critical value when the stressing rate is highest, so stick-slip events should be correlated with peak stressing rate. Since stressing rate increases with increasing frequency, the amplitude necessary for correlation decreases with increasing frequency. This is the regime representing by the decreasing correlation threshold on the left side of Figure 3. The amplitude of stress $\Delta\tau$ necessary for correlation as a function of frequency f , constant stressing rate $\dot{\tau}$, and number of stick-slip events N is given in equation (2). The choice of 0.005 comes from choosing a 99.5% chance of non-randomness as the cutoff between correlated and not correlated

$$\Delta\tau > \sqrt{\frac{-\ln(0.005)}{N}} \frac{\dot{\tau}}{\pi f} \quad (2)$$

[7] In the second regime, called the nucleation-dominated regime, the period of loading is less than the nucleation time of a stick-slip event. In this more complicated case, the rate-and-state theory of *Dieterich* [1992, 1994] predicts that stick-slip events should be correlated with peak stress, rather

than peak stressing rate as in the Coulomb regime. The correlation amplitude is also predicted to not depend on frequency. For a full discussion and derivation, see *Beeler and Lockner* [2003]. The constant amplitude of stress $\Delta\tau$ necessary for correlation is given in equation (3). Here a ($=1/\sigma_{eff} \partial\tau/\partial(\ln V)$) is the rate-and-state parameter as in [*Dieterich*, 1994]. As in the Coulomb regime, the choice of 0.005 comes from choosing a 99.5% chance of non-randomness as the cutoff between correlated and not correlated

$$\Delta\tau > \sqrt{\frac{-\ln(0.005)}{N}} 2a\sigma_{eff} = \sqrt{\frac{-\ln(0.005)}{N}} 2a\mu\tau \quad (3)$$

[8] As effective stress σ_{eff} decreases, as in the tremor region of subduction and strike-slip tectonic environments, the correlation threshold amplitude $\Delta\tau$ decreases in the nucleation dominated response mode (equation (3)) but is unchanged in the threshold failure regime (equation (2)). Consequently, decreasing σ_{eff} should push the intersection of the two modes to higher frequency and shorter period. Equivalently, the nucleation time t_n is shorter in lower effective stress environments. Equations (19a) and (19b) of *Beeler and Lockner* [2003] predict a linear dependence of t_n with σ_n . These equations differ only by a factor of 2π , so here we reproduce only the first equation as equation (4).

$$t_n \approx \frac{2\pi a\sigma_n}{\dot{\tau}} \quad (4)$$

[9] In *Lockner and Beeler* [1999], while experiments were conducted at different axial shortening rates, and thus

Table 1. Summary Table of Experiments Included in This Study and Their Parameters^a

Exp ^b	N ^c	f (Hz)	Amp ^d (μm)	P_p^e (MPa)	P_{rw}	ϕ (deg)	Peak τ^f (MPa)
3	33	0.002	0.7	0.1	0.66		56.5
5	33	0.01	1.3	0.1	0.65		57.3
7	24	0.002	2.7	0.1	0.24		56.4
9	22	0.01	5.3	0.1	5.5 e-4	84.9	57.4
10	40	0.002	2.7	0.1	0.11		54.2
11	50	0.002	5.3	0.1	6.9 e-7	4.6	55.1
12	35	0.01	2.7	0.1	5.0 e-4	64.4	55.7
13	39	0.05	2.7	0.1	0.03		55.1
14	36	0.05	5.3	0.1	0.017		56.2
15	36	0.05	8.0	0.1	0.054		55.8
16	40	0.05	8.0	0.1	0.43		60.6
18	58	0.05	8.0	0	1.5 e-11	106.1	58.1
19a	58	0.002	5.3	20.7	5.6 e-16	-30.2	43.9
19b	35	0.002	2.7	20.7	0.0058		47.1
19c	33	0.002	8.0	20.7	9.6 e-10	21.4	50.3
20a	46	0.01	2.7	20.7	1.2 e-16	94.1	39.9
20b	35	0.01	1.3	20.7	0.055		44.9
20c	30	0.01	0.7	20.7	0.29		48.2
20d	57	0.002	1.3	20.7	0.35		51.4
21a	39	0.004	2.7	20.7	1.6 e-6	34.1	38.1
21b	56	0.004	1.3	20.7	0.032		46.3
21c	35	0.004	0.7	20.7	0.11		48.8
22	53	0.004	1.3	0.1	2.2 e-4	88.9	57.4
23	44	0.004	0.7	0.1	0.83		54.7
24a	41	0.05	5.3	20.7	1.9 e-10	108.9	39.2
24b	61	0.05	2.7	20.7	5.1 e-5	87.3	46.7
24c	26	0.05	8.0	20.7	5.3 e-7	90.9	49.2
24d	66	0.05	1.3	20.7	3.7 e-6	78.1	51.8
25a	35	0.05	1.3	20.7	4.5 e-6	101.4	36.8
25b	74	0.05	0.7	20.7	0.85		46.8

^aNotation: f , P_{rw} , and ϕ are described in the text.^bExperiment number.^cNumber of stick slip events.^dOscillation amplitude.^ePore pressure, 0.1 MPa is used to represent atmospheric pressure.^fMaximum shear stress observed during experiment.

different values of $\dot{\tau}$, all experiments had the same value of σ_{eff} equal to σ_n . In this study, we repeat the experiments of *Lockner and Beeler* [1999] with an axial shortening rate of 0.1 microns/second, but vary σ_{eff} by changing pore fluid pressure. The current experimental setup and sample geometry, shown in Figure 1, is nearly identical to the geometry used in these earlier experiments with the added complexity of controlling pore fluid pressure on the fault. In the original study, experiments were conducted at room dry conditions and a confining pressure of 50 MPa. In our experiments we add deionized water as a pore fluid, with the fault surface fully saturated and connected by a 5 mm diameter bore hole to a reservoir at atmospheric pressure. This arrangement was designed both to confirm the original results and to test if the addition of pore fluid without significant pore pressure had any effect. We conducted additional tests in which pore fluid pressure was maintained at 20.7 MPa, giving an effective confining pressure of 29.3 MPa. This resulted in lower σ_{eff} , while holding constant a and $\dot{\tau}$, providing a new test of the scaling in equation (4).

2. Experimental Methods

[10] Right cylinders of westerly granite were prepared with diameters of 7.62 cm and lengths varying between approximately 15 and 24 cm, with a 30° saw cut to be used

as the sliding surface. In all experiments, samples were deformed in a triaxial loading machine with a constant confining pressure ($\sigma_2 = \sigma_3$) of 50 MPa. A cross-section of the experimental apparatus is shown in Figure 1a. Loading was provided by a hydraulic ram which pushed on the sample from below with a computer-controlled axial shortening rate of 0.1 microns/second. Superimposed on this constant loading was a continuous sine wave, provided by a precision signal generator. This is shown schematically in Figure 1b. The amplitude of these oscillations was converted from volts to microns by calibrating against the actual displacement data.

[11] The saw cut sliding surfaces were consistently prepared prior to each run to ensure uniform starting roughness. Deformation mode and stick-slip characteristics are known to be sensitive to fault surface conditions and careful surface preparation is important in providing repeatable results. Saw cut surfaces were first ground flat with a surface grinder to ensure uniform contact during loading. Then the surfaces were roughened by successive lapping with #400 SiC and #600 Al₂O₃ abrasives on glass plates. After the surfaces were cleaned of the abrasive, the sample halves were inserted into a polyurethane jacket that was then secured to steel end pieces with metal clamps. The sample assembly was then placed in the pressure vessel of the triaxial machine, which contained silicon oil as a confining fluid, and was pressurized to 50 MPa. A greased 1.3 mm Teflon shim was placed between the piston and end piece to allow easy lateral slip during deformation. A vacuum pump was connected to the pore fluid input line (see Figure 1a) and a vacuum applied for a minimum of 5 min to remove air within the saw cut and pore space.

[12] Deionized water was then allowed to enter the sample via a 5 mm bore hole drilled in the top granite half, terminating at the sliding surface. Pore fluid was pressurized to 10 MPa for 10 min, to allow the pore space near the sliding surface to become fully saturated. For atmospheric pore pressure experiments, we then released the pore pressure and connected the pore fluid line to a bottle reservoir held at room temperature and pressure. For high pore pressure experiments, we raised the pore pressure using a pump to 20.7 MPa, and again let it rest for 10 min to saturate the pore space. The pore fluid pump was left operating for the duration of the experiment to maintain the pressure at 20.7 MPa. Next, the piston was positioned 2 mm from the sample, the desired oscillation signal was connected to the displacement control circuit, and the piston was advanced at the nominal rate of 0.1 microns/s. We record displacement, stress, and pore pressure sampled 10 times per second and averaged over 1 second intervals.

[13] A total of 25 experimental runs were carried out, varying the amplitude and frequency of the oscillatory component of displacement, as listed in Table 1. For experiments 19–21 and 24–25 stick slip events were more frequent, so we periodically stopped the experiment, backed off the ram, changed the frequency and/or amplitude of the oscillatory loading, and restarted the experiment. These separate experiment segments are labeled a–d in order of data acquisition. Over the course of each experiment, the stick-slip events create a fine gouge powder. A fine layer of wet gouge is seen in all samples once removed from the machine, and dry gouge was seen in the dry experiment, #18

(see Table 1). For more information on the triaxial machine setup, see *Lockner and Beeler* [1999].

[14] Once we analyzed these experiments, it became clear that we needed to know the characteristic diffusion time for pore fluid across the sample from the center fluid inlet hole to the edge (see section 4.3). In order to calculate this number we measured permeability k and storage coefficient β_c . To measure permeability and diffusivity, we carried out steady flow, oscillating flow, and pulse-decay tests. A special sample was used for these tests in which both the top and bottom halves contained offset bore holes (with a separate return line for the bottom sample half) to cause flow along the saw cut surface. Entry and exit holes along the center line of the fault were separated by 7.62 cm. The top sample half (“high side”) was connected to the pore fluid pump, while the bottom half of the sample (“low side”) was either open to atmospheric pressure (flow through) or closed to passively measure pore fluid pressure at the other end of the sliding surface (oscillating flow technique). We took measurements of permeability before and after stick-slip at various values of axial shortening. The permeability is expected to drop significantly with fault displacement as the initially bare surfaces (approximately 15 micron RMS surface roughness) wear to form a fine-grained gouge layer that fills the open channel ways between surfaces.

[15] In the steady flow tests a constant flow rate was established and the corresponding pressure difference between the high and low sides was measured. In the pulse decay tests a sudden step in pore pressure was introduced on the high side, propagated through the gouge on the sliding surface, and was measured on the low side of the sample. The pore pressure measured on the low side exponentially approached the step value, giving a direct estimate of the diffusion time and allowing for measurement of the permeability k . In the oscillating flow tests, a sine wave in pore pressure was applied on the pump side of the sample. The other side measured a sine wave in pressure that was of lower amplitude, and shifted relative to, the input sinusoid. This can be used to measure both storage coefficient β_c and k , following the methods of *Kranz et al.* [1990] and *Fischer and Paterson* [1992]. β_c is defined as the fractional change in volume per change in pore pressure and has units of MPa^{-1} .

[16] To estimate β_c and k , we assume parallel flow in a channel on the fault plane 1 inch wide by 3 inches long with height (gouge thickness) of 30 microns. Although this is an overly simplistic model, it should give an order of magnitude estimate of these parameters and the total diffusion time Δt (see section 4.3).

3. Analysis Methods

[17] Following *Lockner and Beeler* [1999] and *Beeler and Lockner* [2003], we employ the Schuster test to evaluate each experimental run for correlation with the imposed oscillatory stress signal [*Schuster*, 1897]. Each experiment can be represented as a walk, where each event is represented as a walk segment with unit length and a phase angle. The phase angle refers to the imposed sine wave in displacement and stress, with 0° representing peak stressing rate and 90° representing peak stress. Examples of such walks can be seen in Figure 4. To determine if each experimental run is correlated with the oscillating stress, we test

whether it is well modeled by a random walk. If the walk is random, it will wander an average distance $D = \sqrt{N}$ from the origin. The probability of a random walk ending at a distance D or longer from the origin is given by:

$$P_{rw} = \exp(-D^2/N) \quad (5)$$

[18] We define correlated populations as those where $P_{rw} < 0.005$. For correlated populations, we determine a correlation phase ϕ by performing a least squares fit to the data to a line with zero intercept. The angle of this line is ϕ . Figure 4 shows two walks, one correlated close to 0° and one close to 90° , along with the fit lines representing the correlation phase.

[19] The resolving power of the Schuster test improves with increased sample size in a manner similar to the standard error estimator. To understand this, consider the extreme case of a purely deterministic system that always gives the same outcome; for example flip a coin that always comes up heads. According to equation (5) the probability that this outcome is random after 5 attempts is $P_{rw} = \exp(-5^2/5) \approx 0.0067$. After six attempts, the chance that this is random decreases to 0.0025, and after 10 attempts the probability that 10 heads occur (for a null hypothesis that the system is random) is only 0.000045. While the Schuster test is sensitive to sample size, all sample sizes used in this study are within a factor of 2, and we observe differences in P_{rw} as large as an order of magnitude for highly correlated experiments with the same parameters (see Table 1, experiments #24d and #25a). The bias of the Schuster test is therefore a secondary effect which does not make a large difference for the purposes of this study.

4. Results and Discussion

4.1. Shift of Nucleation Time With Effective Normal Stress

[20] Summary plots of the results of our experiments are shown in Figures 5a and 5b. Open circles represent experiments in which stick slip events were uncorrelated with the periodic loading, while shaded circles represent correlated experiments. The color of shading represents the phase angle of the stress oscillations with which the events are correlated. Angles near 0° (blue colors) represent correlation with peak shear stressing rate $\dot{\tau}$. Angles near 90° (orange colors) represent correlation with peak stress τ . Interpreted in the context of equations (2) through (4) the shift from blue to orange colors thus represents the shift from the Coulomb threshold failure regime to the nucleation dominated failure regime, and constrains t_n . Possible correlation threshold boundaries (see equations (2) and (3)) are shown as black lines in Figures 5a and 5b. An estimate of t_n based on the 0° to 90° phase shift and correlation boundary is also shown as a vertical black line.

[21] For experiments with 50 MPa confining pressure with atmospheric pore pressure (Figure 5a) the peak effective normal stress on the fault is ≈ 81 MPa. In these experiments t_n is estimated from the location of the correlation boundary and 0° to 90° phase angle shift on Figure 5 to be 285 s. The possible range of t_n that explains the data shown in Figure 5a is 255–500 s. For experiments with 50 MPa confining

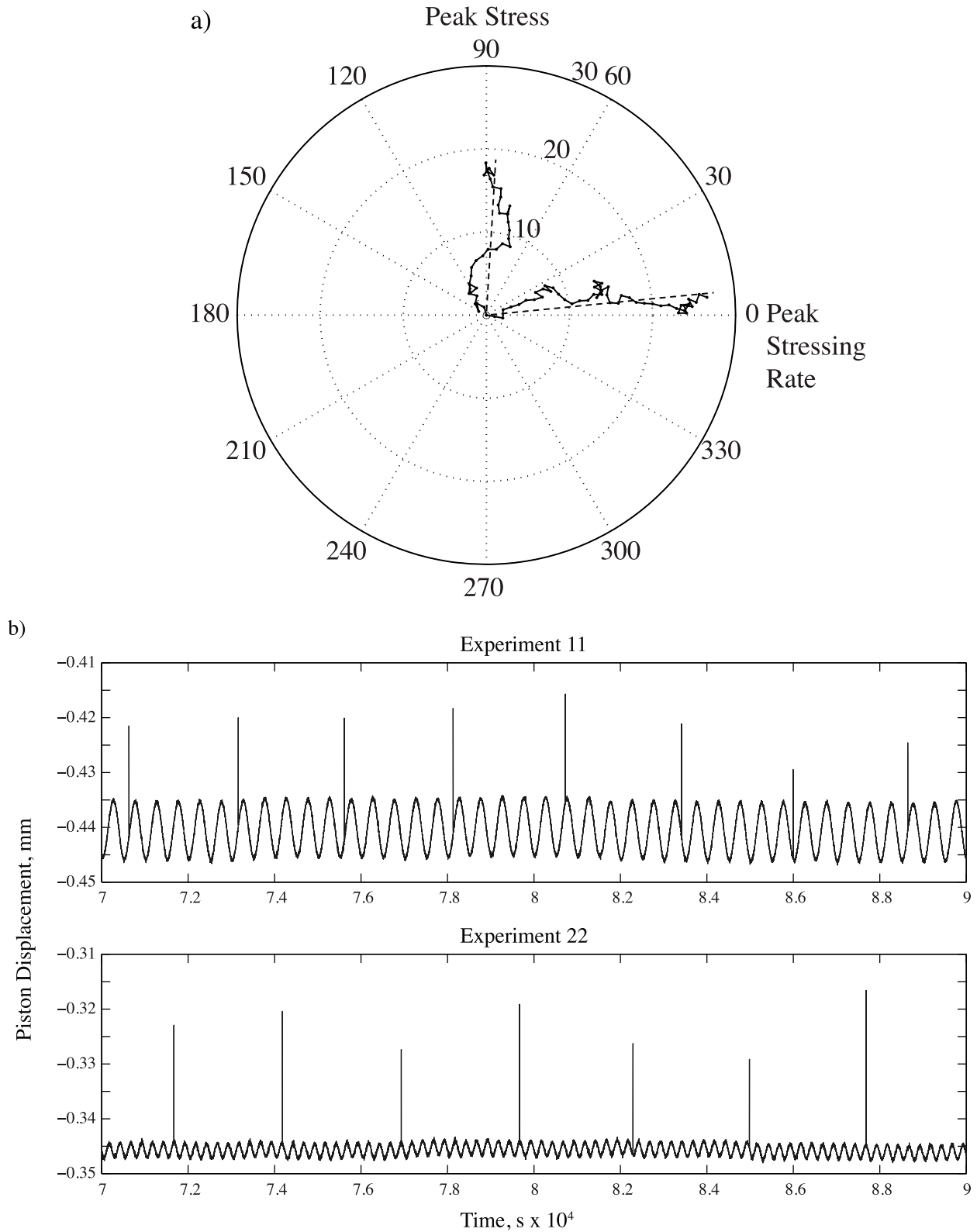


Figure 4. (a) Walks with line fits for two experimental runs. Radial axis represents walk distance, with each step having length 1. The first experiment shown, number 11, is correlated at 4.6 degrees, and has 50 events with $P_{rw} = 6.7 \times 10^{-7}$. The second experiment, number 22, is correlated at 88.9 degrees and has 53 events with $P_{rw} = 3.3 \times 10^{-4}$. (b) Piston displacement for a subset of time from experiments 11 and 22. The linear displacement from the $0.1 \mu\text{m}$ constant loading rate has been removed. Sudden jumps in displacement represent stick-slip events, followed by a correction back to the prescribed piston displacement. The sine wave can be easily seen, and a phase assigned to each event.

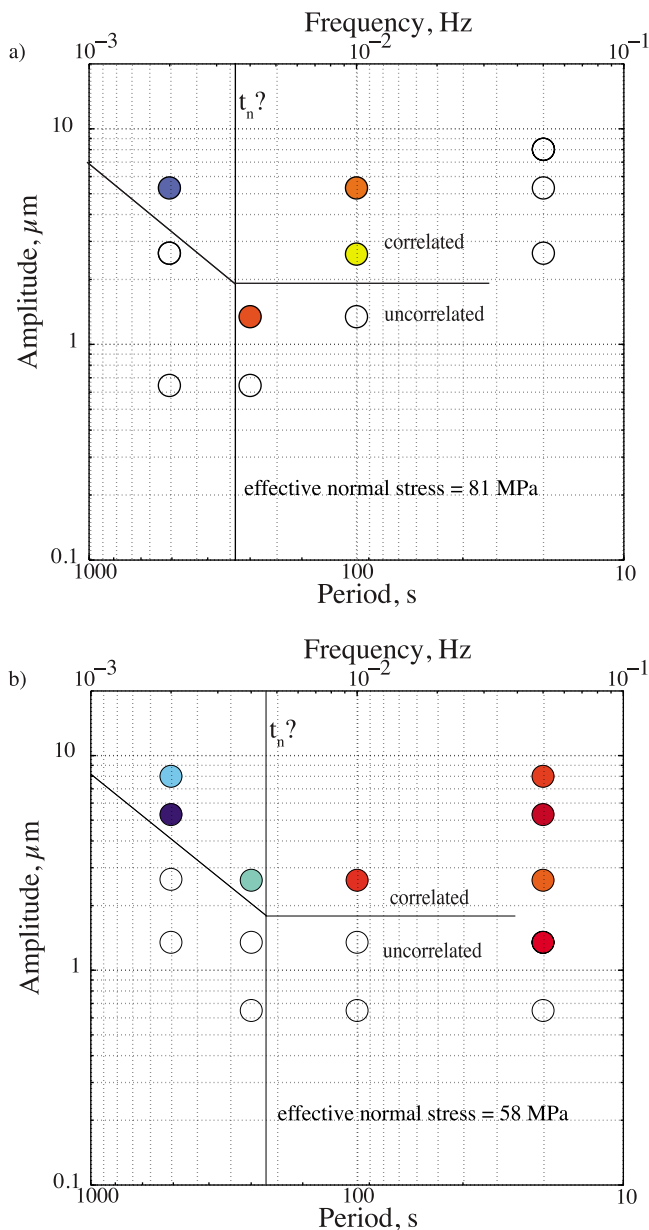


Figure 5. Summary plots of experiments. (a) Wet, 1 atmosphere pore pressure experiments. Same symbols and colors as Figure 3. (b) Wet, 20.7 MPa pore pressure experiments. Same symbols and colors as Figure 3.

pressure and 20.7 MPa pore pressure (Figure 5b) the peak effective normal stress on the fault is ≈ 58 MPa. In this lower effective stress case t_n is estimated to be 220 s, with a possible range of 100–245 s. The predicted shift in t_n from equation (4) is equal to the ratio of effective normal stress, or about a factor of 0.72 from the high effective stress case to the low effective stress case. The estimated values of t_n give a shift of 0.77, with a possible range of 0.2–0.96, in agreement with the predicted shift. We therefore conclude that the nucleation time of stick slip events is dependent on effective normal stress, and these experiments provide strong evidence for the validity of equations (4) and (1).

4.2. Initial Experimental Observations

[22] Some immediate observations of the experiments can be made by looking at the evolution of coefficient of friction μ (calculated as τ/σ_{eff} on the saw cut surface) as a function of shortening distance. Figure 6 shows representative experiments for room-dry, atmospheric pore pressure, and high (20.7 MPa) pore pressure cases. Sudden drops in μ indicate stick-slip events. In dry experiments, strength drops during stick slip events start out small ($\Delta\mu \approx 0.02$) and grow larger ($\Delta\mu \approx 0.15$). In wet experiments, some sequences show a short growth phase, but many begin with near-maximum strength drops. In all cases, wet experiments show far more consistent stress drops with amplitude near the maximum amplitudes of dry experiments. Both wet with atmospheric pore pressure and dry experiments show similar peak coefficient of friction, $\mu \approx 0.65$. In experiments with high pore pressure, stress drops first shrink and then remain small. Later parts of these experiments show small stress drops ($\Delta\mu \approx 0.03$) and high peak friction ($\mu \approx 0.83$). The magnitude of the stress drops for high pore pressure tests is about 20% of the stress drops in the dry and low pore pressure tests. These differences are illustrated in Figure 6. Peak shear stress is about 56 MPa in all wet, 1 atm pore pressure runs, and is lower but grows with fault displacement in the high pore pressure runs (Table 1). This growth can be seen in experiments 19–25, where the progression of letters a–d indicates increasing fault displacement. This growth is also apparent in the increasing peak frictional coefficient μ in the 20.7 MPa case in Figure 6. The dynamic shear stress drops during stick slip at the end of the high pore pressure runs are small ($\Delta\tau = 2.0$ – 3.6 MPa) when compared to dry or low pore pressure runs ($\Delta\tau \approx 17$ MPa). This is equivalent to shear stress drops of about 30% in relative terms for dry and low pore pressure runs and 5%–20% for high pore pressure runs, not including the initial few stick-slip events.

[23] From these experiments, it is unclear if the above observations are due solely to the change in effective pressure, or specifically a fluid pressure effect. At first glance, it might appear that the changing peak friction implies that the

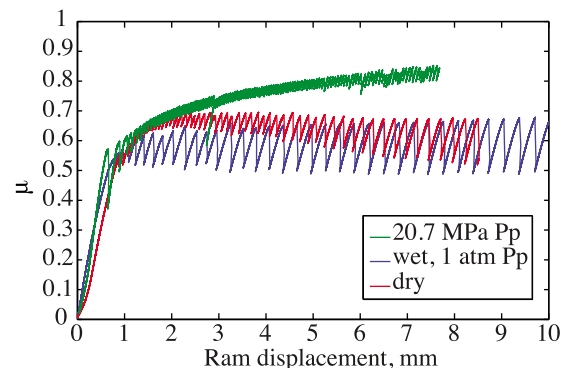


Figure 6. Comparison of friction drops from dry, wet with no pore pressure, and high (20.7 MPa) pore pressure experiments. All experiments shown have imposed oscillatory displacements with 20 s period. The dry and atmospheric pore pressure experiments have constant imposed oscillation amplitude of $16 \mu\text{m}$, and the 20.7 MPa pore pressure experiment has $10.6 \mu\text{m}$, $5.3 \mu\text{m}$, and $16 \mu\text{m}$ amplitude oscillations in the first, middle, and last segments respectively.

effective pressure law (equation (1)) does not hold. However, this change in friction may occur in dry samples where the confining pressure is varied. If this is true, the effective pressure law is not violated. Preliminary investigations show that this is likely the case, however such a discussion is beyond the scope of this paper.

[24] We observe a decrease in stress drops as effective pressure decreases and the system approaches stable sliding. We attempted an experiment with 50 MPa confining pressure and 40 MPa pore pressure, for an effective pressure of 10 MPa, but were unable to produce stick-slip and instead observed stable sliding. The difference in stress drop evolution between dry and 1 atm pore pressure samples is likely due to differences in gouge formation. The evolution of stress drops and peak strength in the dry system is attributed to gouge formation, and the samples begin the experiment nominally gouge free but have gouge after the experiment is completed. It appears that wet systems behave for the entire experiment similarly to dry systems after enough displacement has occurred to form gouge. This implies the water is both mimicking the effects of gouge and inhibiting new gouge formation. Neither the stress drop evolution nor the peak strength of the high pore pressure experiments are currently understood.

4.3. Diffusion of Pore Fluid Pressure

[25] The results shown in Figure 5a that have low, 1 atm pore pressure, are directly comparable to previous room-dry results of *Lockner and Beeler* [1999]. Both sets of experiments have the same confining pressure (50 MPa), the same axial shortening rate (0.1 microns/s), and the same sample size of westerly granite. Both sets of experiments test various oscillatory loading amplitudes at periods of 20, 100, and 500 s. The difference between these experiments is the addition of pore fluid at atmospheric pressure in Figure 5a. Of the three periods in which we have data for both room-dry and atmospheric pore pressure (“wet”) experiments, the correlation threshold matches at two of them. Specifically, we found the same correlation boundary for the 500 s and 100 s data. At 20 s, the wet experiments did not correlate with the oscillatory loading at amplitudes up to 8.0 μm . Since the dry experiments shown in Figure 3 did correlate at an amplitude of 5.3 μm , we ran a room-dry sample at an oscillation amplitude of 8.0 μm (#18; see Table 1) and confirmed that stick-slip events in these conditions are highly correlated with the oscillating load. Therefore, the lack of correlation at the 20 s period must be an effect of the pore fluid, even though the pore pressure is very low. Additionally, the 20.7 MPa pore pressure experiments show a similar effect at the 20 s period, but of opposite sign: experiments were correlated with stress oscillations at anomalously low amplitudes. This effect was confirmed with repeated experiments (see Table 1).

[26] Because this pore fluid effect only appears at high oscillatory stressing frequencies, we hypothesized that the 20 s period experiments represented a new test regime in which pore pressure oscillations were faster than the pore fluid diffusion time for the fault. Given the sample test geometry, oscillations in axial displacement result in oscillations in both shear and normal stress on the fault surface and associated variations in pore volume in the fault. Since the pore fluid in the fault communicates with the external

pore pressure system through a single borehole (Figure 1), changes in pore pressure induced by changes in stress applied to the fault will dissipate according to the diffusion equation

$$\frac{\partial p}{\partial t} = \alpha \left[\frac{\partial^2 p}{\partial x^2} + \frac{\partial^2 p}{\partial y^2} \right] \quad (6)$$

where $\alpha = k/(\beta_c \nu)$ is the diffusion coefficient, k is permeability, ν is dynamic viscosity and β_c is storage coefficient. For most experiments, stresses vary slowly enough that the fault is drained and there is no significant pore pressure build up. However, for rapid stress changes, the fault becomes undrained or partially drained and pore pressure transients will lead to spatial variations in effective normal stress along the fault surface that are no longer represented by the difference between applied normal stress and external pore pressure. To test this hypothesis we performed additional experiments on a modified sample geometry to determine k , β_c and α for the fault (see section 2). Permeability was measured at 0, 5, 7.5 and 10 mm axial shortening, using a steady flow technique (Figure 7). Permeability and storage were measured at 5 and 10 mm shortening by an oscillating flow technique, with the permeability measurements from the two methods showing reasonable agreement (Figure 7). Before sliding, permeability was about $k = 5 \times 10^{-14} \text{ m}^2$ and decreased by 2 orders of magnitude by 5 mm slip. Permeability continued to drop slightly to approximately $3 \times 10^{-16} \text{ m}^2$ by 10 mm slip. The drop in permeability with early sliding is the result of breakage of the rough, interlocked surfaces and rapid grain comminution. As the fault surfaces converge and the fine grained gouge clogs the fault pore space, permeability is dramatically reduced.

[27] The oscillating flow technique provides a joint measure of permeability and storage capacity [*Kranz et al.*, 1990; *Fischer and Paterson*, 1992]. Given the constraints of the sample volume and measurement system, we were able to measure β_c at oscillation periods of 400 to 2000 s. Storage coefficient was unexpectedly large, ranging from 0.02 to 0.09 MPa^{-1} , and increased linearly with oscillation period. We attribute this unusual observation to two-stage flow: primary flow in the fault coupled to secondary flow in the low-permeability granite sample ($k_{\text{granite}} \approx 5 \times 10^{-20} \text{ m}^2$). Assuming a fault with width of 30 microns and porosity of 0.1, fault pore volume is approximately 0.03 cm^3 while pore volume of the granite blocks is about 30 times larger. As the period of pressure oscillation increases in the flow tests, pore fluid pressure has time to diffuse farther and farther into the granite resulting in increased storage capacity.

[28] The preceding discussion relates to poroelastic effects in the auxiliary k/β_c tests. We now return to the diffusion time constant during the oscillating stick-slip experiments. Since β_c is frequency dependent, we extrapolate the calibration measurements to a period of 20 s (the rapid oscillations shown in Figure 5) and obtain $\beta_{c,20s} = 0.004 \text{ MPa}^{-1}$. Using $k = 3 \times 10^{-16} \text{ m}^2$ and viscosity of water, $\alpha_{20s} \approx 7.5 \times 10^{-5} \text{ m}^2 \text{ s}^{-1}$. We developed a 2D finite difference model to solve time-dependent pore pressure diffusion from the borehole to the fault surface. Using this diffusivity and the sample fault dimensions, an abrupt change in pressure at the borehole would require 30 s to change the average pore pressure on the fault by 50 percent. The calibration tests

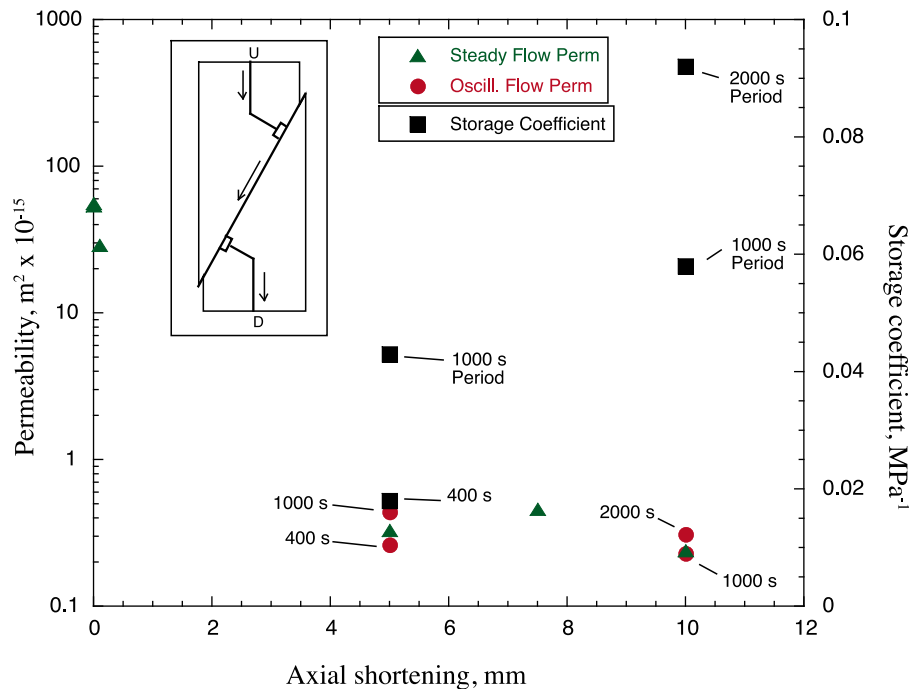


Figure 7. The insert illustrates the modified test geometry for measuring permeability, storage coefficient and hydraulic diffusivity of the sawcut during sliding. Flow tests were conducted at discrete intervals, between 0 to 10 mm, of axial shortening as indicated by horizontal axis in the plot and corresponding to fault slip between 0 and 11.5 mm. For steady flow permeability tests, pore water flows from upstream drill hole ‘U’, along fault, and out downstream hole ‘D’. Oscillating flow test alternately reverses flow direction. Constant flow tests (triangles) and oscillating flow tests (circles) provide consistent measures of permeability. Storage coefficient (squares) increases with the period of oscillating flow cycles. The increased storativity at longer periods appears to be the result of fluid deeper in the granite driving blocks communicating with the sawcut. Under these conditions, permeability of the bulk granite is significantly less than permeability of the sawcut, causing pore pressure changes to diffuse away from the sawcut (see text).

show that more complex modeling is needed to accurately represent the full 3D coupled poroelastic response of the fault/rock system. However, this simple calculation suggests that the anomalous triggering response that occurs at the highest test frequency is apparently associated with pore pressure transients resulting from partial drainage of the fault. The undrained pore fluid at these high frequencies should make the sample less sensitive to normal stress changes, because in an undrained sample, as normal stress increases, pore fluid pressure also increases in a proportion related to the Skempton coefficient. The result is a reduced change in effective normal stress and therefore Coulomb stress.

[29] This poroelastic effect partially explains our anomalous data at 20 s period shown in Figures 5a and 5b. In both cases, the correlation threshold is shifted significantly from the expected value, although in different directions. If pore fluid does not have time to equilibrate at 20 s period, then trapped pore fluid induces higher pore pressure at time of higher normal stress, and lower pore pressure at times of lower normal stress. This has the effect of damping oscillations ineffective stress, making the changes smaller, thus pushing the correlation amplitude higher. While oscillation amplitude is expressed in microns of axial displacement, variations in displacement can be related to corresponding

changes in shear and normal stress on the fault. A two micron oscillation in axial shortening (nucleation threshold in Figure 5) results in approximately 0.12 and 0.07 MPa oscillations in shear and normal stress, respectively. Thus, pore pressure transients in the 0.1 to 0.5 MPa range would be required to shift the correlation threshold by the amounts observed in Figure 5. We do not yet understand why the lower effective stress experiments’ correlation threshold is shifted down, instead of up as in the argument above and as in higher effective stress case.

4.4. Constraints on Physics of Tremor

[30] Our results shown in Figure 5 provide strong evidence that equation (4) captures the correct variation of nucleation time with effective stress and is valid in high pore pressure environments. It can therefore be used to extrapolate nucleation times in deep subduction and strike-slip environments where tremor is observed.

[31] In Japan, tidally modulated tremor appears to be correlated with a phase between peak stress and peak stressing rate, implying that tidal periods of 12 and 24 hours are close to the nucleation time t_n of tremor sources [Nakata *et al.*, 2008]. In Cascadia, tremor appears to be correlated with peak stress, and not peak stressing rate, implying that tremor nucleation times are greater than tidal periods

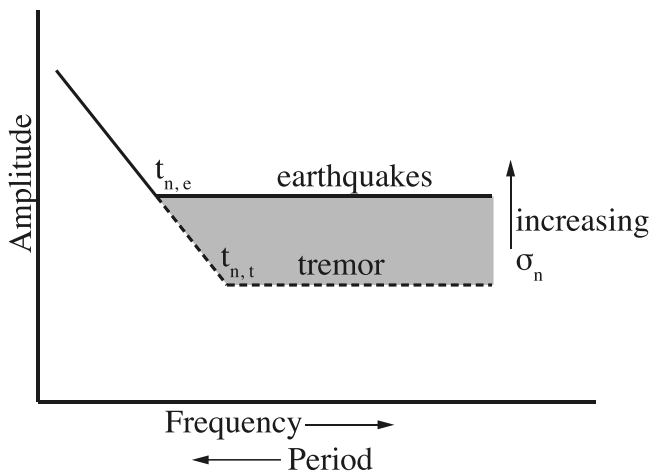


Figure 8. Cartoon of the effect of lower effective stress on the correlation threshold of tremor as compared to regular earthquakes. Increasing σ_n raises the threshold in the nucleation dominated regime but leaves unchanged in the Coulomb threshold triggering regime. The shaded region represents values of the frequency and amplitude of tidal loading that match the observation of tidally modulated tremor but not tidally modulated earthquakes.

[Lambert *et al.*, 2009]. Deep tremor on the San Andreas fault near Parkfield is similarly correlated with peak shear stress, rather than shear stress rate [Thomas *et al.*, 2012].

[32] As discussed in section 1, there is evidence for high pore pressures in the tremor zone. High pore pressures in the tremor zone lower effective stress σ_n , decreasing the nucleation time in equation (4), and decreasing the amplitude for tidal correlation in the nucleation dominated regime in equation (3). The correlation amplitude in the threshold regime is unchanged (equation (2)).

[33] In Japan stressing rates on tremor source patches during slow slip are estimated to be around 5 kPa/day [Nakata *et al.*, 2008]. Effective normal stress in slow slip and tremor regions is thought to be around 1 MPa, with non-dimensional frictional parameter a near 0.004 [e.g., Rubin, 2011]. Plugging these values into equation (4) yields $t_n = 5$ days, within an order of magnitude of tidal periods. This fits well with the observations in Japan, Cascadia, and Parkfield of tremor tidal correlation phases. This estimate of t_n is also close to the 18 hours estimated for tremor on the San Andreas by Thomas *et al.* [2012]. Nucleation times for earthquakes occurring shallower than tremor in the same tectonic setting are expected to be longer due to higher values of normal stress. This places earthquakes firmly in the nucleation dominated regime for tidal loading periods. Additionally, where earthquakes do correlate with solid earth tides, they correlate with peak stress and not peak stressing rate [Cochran *et al.*, 2004; Tsuruoka *et al.*, 1995], confirming the nucleation dominated regime. Values of tidal frequency and amplitude in the shaded region of Figure 8 match the observation that tremor shows strong correlation with tides but regular earthquakes are at best weakly correlated (at about the 10^{-2} level).

[34] It is important to note two alternative explanations for correlation with peak tidal stress in nature. In the Coulomb triggering regime, if the amplitude of tidal stressing rates is

larger than the background stressing rate, then stress reversals are expected during the tidal unloading phase. In a Coulomb triggering model, no events should be triggered during times of decreasing stress or, if there are reversals, during the time of increasing stress before the stress exceeds its previous maximum value. This time of increasing stress in which triggering is prohibited is the shadow of the reversal. If these stress reversals are large enough, it is possible to put the time of peak stressing rate in the shadow region, shifting the correlation phase toward the time of peak stress rather than peak stressing rate. The observed correlation phase in such a case should be in between 0° and 90° on Figures 4 and 5.

[35] A second explanation for an apparent correlation with stress rate in the Coulomb regime occurs if there is an intermediary process between tides and tremor. For example, in the case of tremor accompanying slow slip events, individual tremor patches are likely loaded by creep (slow slip) in the surrounding region. Recent evidence suggests that aseismic slow slip is tidally modulated [Hawthorne and Rubin, 2010], but the correlation phase is not well resolved. It is possible that the aseismic slip rate is modulated by the tides in such a way that there is a phase shift between the stress due to aseismic slip and the stress due to the solid earth tide. In this case there will be an apparent correlation of tremor with tidal stresses at a phase angle that is different from the actual triggering phase angle. Any model for stressing of a tremor patch needs to include tidal stressing from the direct solid earth and ocean tides, plus the stress from the tidally modulated surrounding creep. This is a significantly more complicated problem than the simple sine wave loading scenario considered in this paper.

5. Summary

[36] Our results confirm the prediction of Beeler and Lockner [2003], shown in equation (4), for the scaling of the nucleation time with effective stress. We also confirmed that the previous results of Lockner and Beeler [1999] are valid for experiments with the same effective pressure, but the addition of low-pressure pore fluid. Pore fluids appear to have almost no effect on nucleation time or correlation threshold, except at high frequencies/low periods relative to the diffusion time over the nucleation area. We conclude that lower effective stress due to higher pore pressure is a good explanation for why tidal stresses affect tremor more than regular earthquakes.

[37] **Acknowledgments.** Noel Bartlow is supported by an NSF Graduate Research Fellowship and a Stanford Gabilan Graduate Fellowship. The authors would like to thank Greg Hirth, Allan Rubin, David Shelly, Ole Kaven, and Paul Segall for helpful reviews and discussion.

References

- Audet, P., M. G. Bostock, N. I. Christensen, and S. M. Peacock (2009), Seismic evidence for overpressured subducted oceanic crust and megathrust fault sealing, *Nature*, 457(7225), 76–78, doi:10.1038/nature07650.
- Beeler, N. M., and D. A. Lockner (2003), Why earthquakes correlate weakly with the solid Earth tides: Effects of periodic stress on the rate and probability of earthquake occurrence, *J. Geophys. Res.*, 108(B8), 2391, doi:10.1029/2001JB001518.
- Byerlee, J. D. (1967), Frictional characteristics of granite under high confining pressure, *J. Geophys. Res.*, 72(14), 3639–3648, doi:10.1029/JZ072i014p03639.

- Cochran, E. S., J. E. Vidale, and S. Tanaka (2004), Earth tides can trigger shallow thrust fault earthquakes, *Science*, *306*(5699), 1164–1166, doi:10.1126/science.1103961.
- Dieterich, J. H. (1992), Earthquake nucleation on faults with rate- and state-dependent strength, in *Earthquake Source Physics and Earthquake Precursors*, edited by T. Mikumo et al., pp. 115–134, Elsevier Sci., New York.
- Dieterich, J. (1994), A constitutive law for rate of earthquake production and its application to earthquake clustering, *J. Geophys. Res.*, *99*(B2), 2601–2618, doi:10.1029/93JB02581.
- Fischer, G. J., and M. S. Paterson (1992), Measurement of permeability and storage capacity in rocks during deformation at high temperature and pressure, in *Fault Mechanics and Transport Properties of Rocks*, edited by B. Evans and T.-F. Wong, pp. 213–252, Academic, London.
- Hawthorne, J. C., and A. M. Rubin (2010), Tidal modulation of slow slip in Cascadia, *J. Geophys. Res.*, *115*, B09406, doi:10.1029/2010JB007502.
- Heaton, T. H. (1982), Tidal triggering of earthquakes, *Bull. Seismol. Soc. Am.*, *72*, 2181–2200.
- Kodaira, S., T. Iidata, A. Kato, J.-O. Park, T. Iwasaki, and Y. Kaneda (2004), High pore fluid pressure may cause silent slip in the Nankai trough, *Science*, *304*(5675), 1295–1298, doi:10.1126/science.1096535.
- Kranz, R. L., J. S. Saltzman, and J. D. Blacic (1990), Hydraulic diffusivity measurements of laboratory rock samples using an oscillation pore pressure method, *Int. J. Rock Mech. Min. Sci. Geomech. Abstr.*, *27*(5), 345–352, doi:10.1016/0148-9062(90)92709-N.
- Lambert, A., H. Kao, G. Rogers, and N. Courtier (2009), Correlation of tremor activity with tidal stress in the northern Cascadia subduction zone, *J. Geophys. Res.*, *114*, B00A08, doi:10.1029/2008JB006038.
- Lockner, D. A., and N. M. Beeler (1999), Premonitory slip and tidal triggering of earthquakes, *J. Geophys. Res.*, *104*(B9), 20,133–20,151.
- Nakata, R., N. Suda, and H. Tsuruoka (2008), Nonvolcanic tremor resulting from the combined effect of Earth tides and slow slip events, *Nat. Geosci.*, *1*, 676–678, doi:10.1038/ngeo288.
- Peacock, S. M., N. I. Christensen, M. G. Bostock, and P. Audet (2011), High pore pressures and porosity at 35 km depth in the Cascadia subduction zone, *Geology*, *39*, 471–474, doi:10.1130/G31649.1.
- Rubin, A. M. (2011), Designer friction laws for bimodal slow slip propagation speeds, *Geochem. Geophys. Geosyst.*, *11*, Q04007, doi:10.1029/2010GC003386.
- Rubinstein, J. L., M. L. Rocca, J. E. Vidale, K. C. Creager, and A. G. Wech (2008), Tidal modulation of nonvolcanic tremor, *Science*, *319*(5860), 186–189, doi:10.1126/science.1150558.
- Savage, H. M., and C. Marone (2007), Effects of shear velocity oscillations on stick-slip behavior in laboratory experiments, *J. Geophys. Res.*, *112*, B02301, doi:10.1029/2005JB004238.
- Schuster, A. (1897), On lunar and solar periodicities of earthquakes, *Proc. R. Soc. London*, *61*, 455–465.
- Shelly, D. R., G. C. Beroza, S. Ide, and S. Nakamura (2006), Low-frequency earthquakes in Shikoku, Japan, and their relationship to episodic tremor and slip, *Nature*, *442*(7099), 188–191, doi:10.1038/nature04931.
- Shelly, D. R., G. C. Beroza, and S. Ide (2007), Complex evolution of transient slip derived from precise tremor locations in western Shikoku, Japan, *Geochem. Geophys. Geosyst.*, *8*, Q10014, doi:10.1029/2007GC001640.
- Thomas, A. M., R. M. Nadeau, and R. Bürgmann (2009), Tremor-tide correlations and near-lithostatic pore pressure on the deep San Andreas fault, *Nature*, *462*(7276), 1048–1051, doi:10.1038/nature08654.
- Thomas, A. M., R. Bürgmann, D. R. Shelly, N. M. Beeler, and M. L. Rudolph (2012), Tidal triggering of low frequency earthquakes near Parkfield, California: Implications for fault mechanics within the brittle-ductile transition, *J. Geophys. Res.*, *117*, B05301, doi:10.1029/2011JB009036.
- Tsuruoka, H., M. Ohtake, and H. Sato (1995), Statistical test of the tidal triggering of earthquakes: Contribution of the ocean tide loading effect, *Geophys. J. Int.*, *122*, 183–194.
- Vidale, J. E., D. C. Agnew, M. J. S. Johnston, and D. H. Oppenheimer (1998), Absence of earthquake correlation with Earth tides: An indication of high preseismic fault stress rate, *J. Geophys. Res.*, *103*(B10), 24,567–24,572.
- Wilcock, W. S. D. (2001), Tidal triggering of microearthquakes on the Juan de Fuca Ridge, *Geophys. Res. Lett.*, *28*(20), 3999–4002, doi:10.1029/2001GL013370.